Turbulent transport of heat and particles in a high ion temperature discharge of the Large Helical Device

Turbulent transport of heat and particles in a high ion temperature discharge of the Large Helical Device

A. Ishizawa, T.-H. Watanabe[1], H. Sugama, M. Nunami, K. Tanaka, S. Maeyama[2], and N. Nakajima

National Institute for Fusion Science, Toki, 509-5292, Japan
[1]Department of Physics, Nagoya University, Nagoya, 464-8602, Japan
[2]Japan Atomic Energy Agency, Kashiwa, 277-8587, Japan

E-mail: ishizawa@nifs.ac.jp

Abstract. Turbulent transport in a high ion temperature discharge of the Large Helical Device (LHD) is investigated by means of electromagnetic gyrokinetic simulations, which include kinetic electrons, magnetic perturbations, and full geometrical effects. Including kinetic electrons enables us to firstly evaluate the particle and the electron heat fluxes caused by turbulence in LHD plasmas. It is found that the electron energy transport reproduces the experimental result, and that the particle flux is negative. The contribution of magnetic perturbation to the transport is small because of very low beta. The turbulence is driven by the ion temperature gradient (ITG) instability, and the effect of kinetic electrons enhances the growth rate larger than that from the adiabatic electron calculation. The ion energy flux is larger than that observed in the experiment, while the flux is close to the experimental observation when the temperature gradient is reduced 20% in the simulation. This significant sensitivity of the energy flux implies that the profile in the experiment is close to the critical temperature gradient. The critical gradient for turbulent energy flux is similar to that for the linear instability, i.e., the Dimits shift is small. This is because the zonal flow in the LHD is weaker than that in tokamaks.

PACS numbers: 52.35.Ra, 52.65.Tt, 52.25.Fi, 52.35.Mw

1. Introduction

Helical plasmas in heliotron and stellarator systems are confined by an externally produced magnetic field, and thus are advantageous in maintaining a steady discharge. The confinement of the helical plasmas is optimized to reduce the MHD instability and the neoclassical transport by utilizing the freedom of three dimensionality, and further optimization is expected by improving anomalous transport due to turbulence driven by micro-instabilities [1] [2]. The turbulent transport is normally larger than the neoclassical transport in helical plasmas, and thus it is one of the critical issues of the confinement. The gyrokinetic analysis is applied to the turbulent transport in helical plasmas [3, 4, 5, 6, 7, 8, 9, 10, 11, 12, 13] as well as the turbulent transport in tokamak plasmas [14, 15, 16, 17, 18, 19, 20, 21, 22, 23, 24, 25, 26, 27, 28, 29, 30].

The Large Helical Device (LHD) is a heliotron system that confines a plasma by a magnetic field produced by two helical coils [31]. Most gyrokinetic simulations of helical plasmas are carried out in a flux tube geometry, and they require much more computational resources than those of tokamak plasmas because the large number of grid-points along the magnetic field line is needed to capture the helical ripple structure. The turbulent transport in model configurations of LHD plasmas is studied by means of gyrokinetic simulations with the adiabatic electron model [5], and it is found that an optimization of magnetic field configuration against the neoclassical transport improvement enhances the zonal flow production. Thus, the optimization improves the turbulent transport due to ion temperature gradient (ITG) modes through the interplay between the ITG turbulence and the zonal flows. The study is extended to include the kinetic electrons and the magnetic perturbations, and reveals that the finite beta effects reduce the growth of the ITG mode, and the kinetic ballooning mode (KBM) is destabilized when the beta exceeds 2% or 3% [10]. The most unstable KBM has a finite ballooning angle, and its mode structure causes a new saturation mechanism of the KBM turbulence which normally produces very weak zonal flows [12]. The new saturation mechanism is significant in high beta helical plasmas. A validation of the gyrokinetic simulation with the adiabatic electron is carried out for a high ion temperature discharge of LHD (discharge number 88343) [9]. It is found that the ion heat flux caused by the ITG turbulence is in good agreement with the experimental observation.

The effects of kinetic electrons normally enhance the growth rate of ITG modes [15, 32], while the finite beta effects reduce the growth rate of the ITG modes [13, 16, 18, 37], and thus validation including these effects is important. In this work, the electromagnetic gyrokinetic analysis is applied to the high ion temperature discharge of LHD #88343 to clarify the effects of kinetic electrons and finite beta.

The paper is organized as follows. The numerical simulation model and the profiles of the temperatures, the density and the magnetic field of LHD discharge #88343 are described in Sec. 2. Results by linear analysis are given in Sec. 3. Nonlinear simulation results are presented in Sec. 4. And, summary is given in Sec. 5.

2. Simulation model

The profiles used in this paper are described here. The ion and electron temperature profiles at $t = 2.2[s]$ of LHD #88343, which is a high ion temperature discharge [34], are shown in Fig. 1. The temperatures are higher than 3 [KeV] at the core, and the density is about $1 \times 10^{19}[m^{-3}]$. The plasma beta is about 0.4 % at the core, and the safety factor decreases from 2.8 at the magnetic axis to 0.8 at the edge. The magnetic field configuration is obtained from the MHD equilibrium code VMEC [35]. Parameters for the gyrokinetic simulations at $\rho = 0.46$, 0.65, and 0.83 are listed in Table 1.

We consider micro-turbulence in a flux tube that is along a chosen magnetic field line represented by the coordinates (x, y, z), where $x = \frac{q(\psi_0)}{B_0 r(\psi_0)}(\psi - \psi_0)$, $y = \frac{-r(\psi_0)}{q(\psi_0)}(\alpha - \alpha_0)$, and $z = \theta$, (ψ, θ, ζ) is a flux coordinate, $\alpha = \zeta - q(\psi)\theta$ is the magnetic field line label, ψ is the magnetic flux, θ is the poloidal angle, and the tube is located on a field line with $\psi = \psi_0$ and $\alpha = \alpha_0$ [39]. The gyro-center distribution function for a species s is divided into the Maxwellian and the perturbed parts $f_s(x, y, z, v_\parallel, \mu) = F_{Ms} + \delta f_s$. In the flux tube coordinate system the gyrokinetic equation for the non-adiabatic part of the perturbed part $h_{s\mathbf{k}_\perp} = \delta f_{s\mathbf{k}_\perp} + \frac{q_s}{T_s}\phi_{\mathbf{k}_\perp} J_{0s} F_{Ms}$ is written as

$$\begin{aligned}\frac{\partial h_{s\mathbf{k}_\perp}}{\partial t} = & - v_{Ts} v_\parallel \mathbf{b}\cdot\nabla h_{s\mathbf{k}_\perp} - i\mathbf{v}_{ds}\cdot\mathbf{k}_\perp h_{s\mathbf{k}_\perp} \\ & + v_{Ts}\mu\mathbf{b}\cdot\nabla B\frac{\partial h_{s\mathbf{k}_\perp}}{\partial v_\parallel} + q_s\frac{F_{Ms}}{T_s}\frac{\partial \chi_{s\mathbf{k}_\perp}}{\partial t} \\ & + i\mathbf{v}_{*s}\cdot\mathbf{k}_\perp q_s\frac{F_{Ms}}{T_s}\chi_{s\mathbf{k}_\perp} - [\chi_s, h_s]_{\mathbf{k}_\perp} + C_s(h_{s\mathbf{k}_\perp}),\end{aligned} \tag{1}$$

where $\chi_{s\mathbf{k}_\perp} = (\phi_{\mathbf{k}_\perp} - v_{Ts} v_\parallel A_{\parallel\mathbf{k}_\perp}) J_{0s}$ is the generalized potential, $[\chi_s, h_s]_{\mathbf{k}_\perp} = \sum_{\mathbf{k}'_\perp, \mathbf{k}''_\perp} \delta_{\mathbf{k}_\perp, \mathbf{k}'_\perp + \mathbf{k}''_\perp} \mathbf{b}\cdot\mathbf{k}'_\perp \times \mathbf{k}''_\perp \chi_{s\mathbf{k}'_\perp} h_{s\mathbf{k}''_\perp}$ is the Poisson bracket, $J_{0s} = J_0(\rho_s k_\perp)$ is the zeroth order Bessel function, and $\mathbf{k}_\perp = (k_x, k_y)$. The quantities are normalized as $(tv_{Ti}/R_0,\ \mathbf{k}_\perp\rho_{Ti},\ v_\parallel/v_{Ts},\ F_{Ms}v_{Ts}^3/n_0,\ h_s R_0 v_{Ts}^3/(\rho_{Ti} n_0),\ \phi e R_0/(\rho_{Ti} T_i),\ A_\parallel e R_0/(\rho_{Ti} T_i),\ m_s/m_i,\ T_s/T_i,\ n/n_0,\ B/B_0,\ q_s/e,\ \lambda_{Di}/\rho_{Ti}) \to (t,\ \mathbf{k}_\perp,\ v_{\parallel s},\ F_{Ms},\ h_s,\ \phi,\ A_\parallel,\ M_s,\ T_s,\ n,\ B,\ q_s,\ \lambda_{Di})$, where m_s, T_s, q_s, and $v_{Ts} = \sqrt{T_s/m_s}$ are the mass, the temperature, the electric charge, and the thermal velocity, respectively. The ion Debye length is denoted by $\lambda_{Di} = \sqrt{T_i/(4\pi e^2 n_0)}$ and the leading order of Larmor radius $\rho_i = v_\perp/\Omega_i$ is written as $\rho_{Ti} = v_{Ti}/\Omega_i$, where $\Omega_i = eB/(m_i c)$ is the ion cyclotron frequency. The gyrokinetic Poisson equation for the electrostatic potential ϕ and Ampère's law for the parallel component of the vector potential $A_\parallel$ are

$$\lambda_{Di}^2 k_\perp^2 \phi_{\mathbf{k}_\perp} = \sum_s q_s \left(\int h_{s\mathbf{k}_\perp} J_{0s} d^3 v - \frac{q_s}{T_s}\phi_{\mathbf{k}_\perp} \right) \tag{2}$$

and

$$k_\perp^2 A_{\parallel\mathbf{k}_\perp} = \frac{\beta_i}{2}\sum_s q_s v_{Ts} \int v_\parallel h_{s\mathbf{k}_\perp} J_{0s} d^3 v, \tag{3}$$

respectively, where $\beta_i = 8\pi n_0 T_i/B_0^2$ is the ion beta. The magnetic and diamagnetic drift-velocities are $\mathbf{v}_{ds} = \frac{1}{q_s B}\mathbf{b}\times(\mu\nabla B + m_s v_\parallel^2 \mathbf{b}\cdot\nabla\mathbf{b})$ and $\mathbf{v}_{*s} = \frac{T_s}{q_s B}\mathbf{b}\times\nabla\ln F_{Ms}$, and

the collision operator is denoted by $C_s(h_{s\mathbf{k}_\perp})$. The parallel component of the perturbed magnetic field and the finite beta term in the magnetic drift-velocity are neglected by assuming that the plasma beta is not high. The electromagnetic gyrokinetic equation Eq. (1) for ions and electrons, the Poisson equation Eq. (2), and Ampère's law Eq. (3) are solved by the GKV+ code [40, 10, 41].

3. Linear analysis of micro-instability

Micro-instabilities in the LHD experiment #88343, which is a high ion temperature discharge, are studied in this section. In the simulations, 2560, 128, and 32 grid points are distributed in $-10\pi \le z \le 10\pi$, $-4 \le v_\parallel \le 4$, and $0 \le \mu \le 8$, respectively. It is remarked that the flux tube covers whole full flux surface by setting $-10\pi \le z \le 10\pi$.

Figure 2 shows the growth rate and real frequency of micro-instabilities as a function of the wavenumber in the binormal direction, k_y, at $\rho = 0.46$, 0.65, and 0.83. The instabilities are the ion temperature gradient (ITG) mode because the mode rotates toward the ion diamagnetic direction. The core region $\rho = 0.46$ is more stable than the location near the edge $\rho = 0.83$. The growth rate of the most unstable mode at $\rho = 0.65$ is about two times larger than that at $\rho = 0.46$, and the growth rate at $\rho = 0.83$ is about three times larger than that at $\rho = 0.46$. The wavenumber of the most unstable mode decreases from $k_y\rho_{Ti} \approx 0.4$ at $\rho = 0.46$ to $k_y\rho_{Ti} \approx 0.3$ at $\rho = 0.83$. Figure 3 shows that the electron temperature gradient (ETG) mode is unstable around $k_y \approx 10/\rho_{Ti} \approx 0.25/\rho_{Te}$ at $\rho = 0.65$, and the mode rotates toward the electron diamagnetic direction. Figure 4 shows the profiles of the amplitude of the magnetic field B, the electrostatic potential ϕ, the ion magnetic drift frequency $\omega_{di} = \mathbf{v}_{di} \cdot \mathbf{k}_\perp$, and the norm of the perpendicular wavenumber $|\mathbf{k}_\perp|$ for $(k_x, k_y) = (0, 0.3/\rho_{Ti})$ along the magnetic field line at $\rho = 0.46$, 0.65, and 0.83. The electrostatic potential profile has a peak at $z = 0$ that is the outside of the torus. The profile has a small oscillation due to particles trapped in the helical ripples, which is represented by the amplitude of magnetic field. The ripple has ten cycles for one period along the parallel direction. The period of the ripple is longer at the radial location for smaller q, and the amplitude of the ripple is large in the edge region. The instability has a ballooning structure which is a peaked profile around $z = 0$, and the peaked structure is narrow for strong instability. The ballooning structure is linked to the small amplitude of $k_\perp^2$ and the negative amplitude of the ion magnetic drift frequency, $\omega_{di} < 0$, around $z = 0$. Figure 5 shows that the growth rate from the electromagnetic calculation is about two times larger than that from the adiabatic electron calculation.

Figure 6 shows the growth rate as a function of β at $\rho = 0.65$, where β is changed with using the same the magnetic configuration and density and temperature profiles. The black point represents the growth rate for the experimental value of beta ($\beta = 0.3\%$). The growth rate obtained from the electromagnetic calculation is about two times larger than that obtained from the adiabatic electron calculation indicated by the horizontal cyan line. The increase of the growth rate is attributed to the kinetic

electrons, because the similar increase of the growth rate is observed for the $\beta = 0$ case. The beta of #88343 is so small that the growth rate is close to that for the $\beta = 0$, and thus the effect of magnetic perturbation on the instability is negligible. When the beta is increased with using the same magnetic field, temperature, and density profiles, the growth rate of ITG mode is suppressed by magnetic field line bending effects, while the KBM is destabilized at high beta [36]. The blue open circles represent the growth rate with $k_x = 0$, which has zero ballooning angle $\theta_k = -k_x/(k_y \hat{s}) = 0$. The plasma beta in the experiment is much lower than the critical beta of the KBM, $\beta/\beta_{KBM} \approx 0.08$. The most unstable KBM has a finite radial wavenumber, which is denoted by the red open circles, and this typical feature of KBMs in helical plasmas causes a new saturation mechanism of KBM turbulence, which barely produces zonal flows [12]. The curve of the growth rate is a typical beta dependence of the ITG mode and KBM in torus plasmas [13, 14, 15, 16, 18, 37].

4. Turbulent transport

Nonlinear simulation results at $\rho = 0.65$ are presented in this section. The nonlinear simulations of LHD plasmas require very large computer resources because of the large number of grid-points and Fourier modes in the simulation. The total Fourier mode number in the x direction and the y direction are 256 and 128, respectively, and the total grid-points number in the parallel direction, the parallel velocity direction, and the perpendicular velocity direction are 512, 128, and 32, respectively. Thus, we carried out only one nonlinear simulation for $\rho = 0.65$. The position $\rho = 0.65$ is chosen for its clear linear ITG signature and to avoid any plasma edge effects.

First, we show that a statistical steady state of the ITG turbulence is obtained in terms of the entropy balance. The entropy balance equation, which shows the conservation of a quadratic quantity [42], is written as

$$\frac{d}{dt}(\sum_s T_s \delta S_s^{(h)} + W_{es}^{(h)} + W_{em}) = \sum_s (F_s + D_s), \tag{4}$$

where

$$\delta S_s^{(h)} = \left\langle \sum_{\mathbf{k}_\perp} \int d^3v \frac{1}{2F_{Ms}} |h_{s\mathbf{k}_\perp}|^2 \right\rangle, \tag{5}$$

$$W_{es}^{(h)} = \sum_{\mathbf{k}_\perp} \left\langle \left(\lambda_{Di}^2 k_\perp^2 + \sum_s \frac{q_s^2}{T_s} \right) \frac{|\phi_{\mathbf{k}_\perp}|^2}{2} \right\rangle, W_{em} = \sum_{\mathbf{k}_\perp} \left\langle \frac{2}{\beta_i} \frac{k_\perp^2 |A_{\parallel \mathbf{k}_\perp}|^2}{2} \right\rangle, \tag{6}$$

$$F_s = \mathrm{Re} \left\langle \sum_{\mathbf{k}_\perp} \int d^3v \mathbf{v}_{*s} \cdot i\mathbf{k}_\perp h_{s\mathbf{k}_\perp}^* \frac{q_s}{2} \chi_{s\mathbf{k}_\perp} \right\rangle, \tag{7}$$

$$D_s = \mathrm{Re} \left\langle \sum_{\mathbf{k}_\perp} \int d^3v \frac{T_s}{2F_{Ms}} h_{s\mathbf{k}_\perp}^* C_s(h_{s\mathbf{k}_\perp}) \right\rangle, \tag{8}$$

where $<>$ is the flux surface average and $\mathrm{Re}[f]$ is the real part of f. The time derivative term $d(\sum_s T_s \delta S_s^{(h)} + W_{es}^{(h)} + W_{em})/dt$ and the free energy term F_s are the same as

$d(\sum_s \delta S_s + W_{es} + W_{em})/dt$ and $(\Theta_{es,s} + \Theta_{em,s})/L_{Ts} + (T_s\Gamma_{es,s} + T_s\Gamma_{es,s})/L_{ps}$ in the previous work [10, 12, 13], respectively. Figure 7 shows the time history of each term in the entropy balance equation Eq. (4). The time derivative term is very small on average after $t \approx 35$, and thus the ITG turbulence is in a statistical steady state. In the steady state the ion (electron) free energy term F_i (F_e) almost balances with the ion (electron) collisional dissipation term D_i (D_e).

Figure 8 shows the ion and electron energy fluxes Q_i and Q_e obtained by the electromagnetic simulation, the adiabatic electron simulation, experimental observation, and the anomalous part of the experimental observation, where $Q_s = Q_{es,s} + Q_{em,s}$,

$$Q_{es,s} = \mathrm{Re}\left\langle \sum_{\mathbf{k}_\perp} \frac{1}{2} \int (m_s v_\parallel^2 + \mu B) h_{s\mathbf{k}_\perp} J_{0s} d^3v \left(\frac{-ik_y \phi_{\mathbf{k}_\perp}}{B} \right)^* \right\rangle, \tag{9}$$

$$Q_{em,s} = \mathrm{Re}\left\langle \sum_{\mathbf{k}_\perp} \frac{1}{2} \int v_{Ts} v_\parallel (m_s v_\parallel^2 + \mu B) h_{s\mathbf{k}_\perp} J_{0s} d^3v \left(\frac{ik_y A_{\parallel \mathbf{k}_\perp}}{B} \right)^* \right\rangle. \tag{10}$$

The ion energy flux is saturated around $t \approx 35$ and is in a statistical steady state after $t \approx 40$. The ion energy flux (red line) obtained by the electromagnetic gyrokinetic simulation is about three times larger than the experimentally observed anomalous transport (black line), which is obtained by subtracting the neoclassical transport part from the observed value in the experiment (cyan line). The flux obtained by the adiabatic electron model is indicated by the blue line and is very close to the experimentally observed anomalous part. The electron energy flux, which is the red line, is in good agreement with the anomalous part of the observed value in the experiment. The anomalous part is again obtained by subtracting the neoclassical transport part from the experimental observation. Figure 9 shows the time history of the particle flux $\Gamma = \Gamma_i = \Gamma_e$, where $\Gamma_s = \Gamma_{es,s} + \Gamma_{em,s}$,

$$\Gamma_{es,s} = \mathrm{Re}\left\langle \sum_{\mathbf{k}_\perp} \int h_{s\mathbf{k}_\perp} J_{0s} d^3v \left(\frac{-ik_y \phi_{\mathbf{k}_\perp}}{B} \right)^* \right\rangle, \tag{11}$$

$$\Gamma_{em,s} = \mathrm{Re}\left\langle \sum_{\mathbf{k}_\perp} \int v_{Ts} v_\parallel h_{s\mathbf{k}_\perp} J_{0s} d^3v \left(\frac{ik_y A_{\parallel \mathbf{k}_\perp}}{B} \right)^* \right\rangle. \tag{12}$$

The particle flux is negative, and this implies that the particles are transported toward the magnetic axis by the ITG turbulence, i.e., the electromagnetic ITG turbulence has a pinch effect on particles. The density gradient at $\rho = 0.65$ is slightly negative, so that the particle transport coefficient has positive sign. The particle pinch is also observed in the gyrokinetic simulations for tokamaks, and the sign of the particle flux significantly influenced by the electron-ion collisions, as shown in Ref. [33]. Figure 10 shows the contribution of magnetic perturbation to the energy fluxes and particle flux. The electromagnetic part is very small compared with the electrostatic part because of low beta, $\beta = 0.3\%$. The contribution of magnetic perturbation to the electron energy flux is about 3%, and is larger than that to the ion energy flux, which is negative. Thus the electron energy flux is much more influenced by the magnetic perturbation than the

ion energy flux. The contribution of magnetic perturbation to the particle flux is about 3% and has small pinch effects.

Figure 11 (a) shows the spectrum of the square of the electrostatic potential averaged over the steady state for the LHD 88343. The amplitude of the ITG modes has a peak around $k_y\rho_{Ti} \approx 0.1$ for both electromagnetic and the adiabatic electron simulations. The amplitude of the ITG mode at $k_y\rho_{Ti} = 0.1$, $< |\phi_k(k_y\rho_{Ti} = 0.1)|^2 >$, is comparable with that of zonal component, $< |\phi_k(k_y\rho_{Ti} = 0)|^2 >$. The amplitude of the ITG mode obtained from the electromagnetic simulation is about three times larger than that from the adiabatic simulation around $k_y\rho_{Ti} = 0.1$. That is consistent with the fact that the ion energy flux by the electromagnetic simulation is three times larger than that by the adiabatic electron simulation in Fig. 8. Figure 11 (b) shows the spectrum for the Cyclone base case tokamak, where numerical settings for the CBC is described in Refs. [10, 13]. The amplitude of the zonal component, $< |\phi_k(k_y\rho_{Ti} = 0)|^2 >$, is much larger than that of the ITG mode $< |\phi_k(k_y\rho_{Ti} = 0.2)|^2 >$. Thus, the zonal flow in the LHD is weak compared with the CBC.

Finally, we discuss the sensitivity of the energy flux to the temperature gradient which drives the ITG instability, because the ion energy flux from the simulation is about three times larger than that from the experiment in Fig. 8. Figure 12 shows the linear growth rate and the energy fluxes due to the ITG turbulence driven by reduced temperature gradients. We made concurrent changes in both ion and electron temperature gradients, and the gradient $1/L_{Ts}$ is reduced to $1/L_{Ts} = 0.9/L_{Texp,s}$ and $1/L_{Ts} = 0.8/L_{Texp,s}$ for both of $s = i$ and $s = e$, where $1/L_{Texp,s}$ is the value in Table 1 for $\rho = 0.65$. The x-axis of the figure is the gradient normalized by the experimental value, $L_{Texp}/L_T \equiv L_{Texp,i}/L_{Ti} = L_{Texp,e}/L_{Te}$. The red line represents the linear growth rate obtained from the reduced gradient simulations. The growth rate is normalized by that from the calculation with the experimental value of the gradient $\gamma(L_{Texp})$, which is the largest value in Fig. 5. The threshold of the linear instability is about 60% of the temperature gradient observed in the experiment. The blue (black) line represents the ion (electron) energy flux from the reduced gradient simulations. The fluxes are averaged over the statistical steady state in the simulation and are normalized by the flux with the gradient of the experiment, as $Q_s/Q_s(L_{Texp})$. The energy flux decreases by reducing the gradient, and the ion energy flux with the gradient reduced 20% is close to the experimentally observed value. The electron energy flux decreases, as well. Thus, the energy flux is very sensitive to the temperature gradient. This implies that the temperature profile in the experiment is close to the critical gradient at which turbulence appears. The threshold of the linear instability and that of the energy flux are very close, and thus the Dimits shift is very small. This is in contrast with the CBC tokamak, which has a finite shift [43]. This is because the zonal flow in the tokamak case is stronger than that in LHD 88343, as shown in Fig. 11.

5. Summary

Turbulent transport in a high ion temperature LHD discharge (number 88343) is studied by means of the electromagnetic gyrokinetic simulations as a validation. The plasma is unstable against the ITG mode from the core to the edge, $\rho = 0.46$, 0.65, and 0.83, and the edge region is more unstable than the core region. The kinetic electron effects enhance the growth rate two times larger than that from the adiabatic electron model. The mode structure along the magnetic field line has a ballooning structure with oscillation due to trapped particles in the helical ripples. The reduction of the growth rate by the finite beta effect is negligible because of the very small beta, $\beta = 0.3\%$.

When the beta is increased while keeping the magnetic configuration and the profiles, the kinetic ballooning mode (KBM) becomes unstable above $\beta \approx 3.5\%$. The threshold of the KBM may be influenced by the effect of the parallel component of the perturbed magnetic field $\delta B_{\parallel}$ as shown in Ref. [8]. The most unstable KBM has a finite ballooning angle which corresponds to a finite radial wavenumber in the flux tube coordinate.

In the nonlinear simulation, the turbulent ion energy flux is about three times that of the anomalous part of the experimental observation, while the flux is close to the experimental observation when the temperature gradient is reduced 20% in the simulation. Thus, the local flux tube simulation implies that the energy flux is very sensitive to the temperature gradient, and that the temperature profile realized in the experiment is close to the critical gradient of the ITG turbulence. The turbulent electron energy flux is in good agreement with the anomalous part of the experimental observation. The turbulent particle flux is negative and has pinch effect. The spectrum of the electrostatic potential has a peak at $k_y \rho_{Ti} \approx 0.1$ and the zonal component $k_y = 0$ has a similar level with the peak. Although the amplitude of the zonal flow is comparable with the ITG turbulence, the Dimits shift is small. This is because the zonal flow is weaker than that in the CBC tokamak which exhibits a finite Dimits shift. In helical systems, radial drift motions of particles trapped in helical ripples decrease the radial potential difference and the residual zonal flow level as shown in Refs. [44, 45]. This mechanism is considered to cause weaker zonal flow generation in the LHD case than in the CBC tokamak. In our future work we will carry out nonlinear simulations at the edge region $\rho = 0.83$, so that we will see whether the gyrokinetic study of LHD has the short fall problem [28, 29, 30].

Acknowledgments

The authors thank Dr. M. Yokoyama and Dr. S. Satake for providing the data of neoclassical transport calculation. The work is supported by the Japanese Ministry of Education, Culture, Sports, Science and Technology Grant Nos. 23561003 and 21560861 and by the NIFS Collaborative Research Program (NIFS14KNST067, NIFS14KNTT026, and NIFS14KNTT027). This research uses computational resources

of the Plasma Simulator at NIFS, Helios at IFERC-CSC and K at RIKEN Advanced Institute for Computational Science through the HPCI System Research project (Project ID: hp140044).

References

[1] Xanthopoulos, P., Mynick, H., Helander, P., Turkin, Y., et al., Phys. Rev. Lett. 113, 155001 (2014)
[2] Helander, P., Beidler, C.D., Bird, T.M., M Drevlak, Y Feng, R Hatzky, F Jenko, R Kleiber, J H E Proll, Yu Turkin and P Xanthopoulos, Plasma Phys. Control. Fusion 54 (2012) 124009.
[3] Watanabe, T.-H., Sugama, H., and Ferrando-Margalet, S., Nucl. Fusion 47, (2007) 1383.
[4] Xanthopoulos, P., Merz, F., Gorler, T., and Jenko, F., Phys. Rev. Lett. 99, (2007) 035002.
[5] Watanabe, T.-H., Sugama, H., Margalet, S.F., Phys. Rev. Lett. **100**, (2008) 195002.
[6] Xanthopoulos, P., Mischchenko, A., Helander, P., Sugama, H., and Watanabe, T.-H., Phys. Rev. Lett. 107, (2011) 245002.
[7] Nunami, M., Watanabe, T.-H., Sugama, H., and Tanaka, K., Plasma Fusion Res. 6, (2011) 1403001.
[8] Baumgaertel, J. A., Hammett, G. W., Mikkelsen, D. R., Nunami, M., and Xanthopoulos, P., Phys. Plasmas 19, (2012) 122306.
[9] Nunami, M., Watanabe, T.-H., Sugama, H., and Tanaka, K., Phys. Plasmas **19**, (2012) 042504.
[10] Ishizawa, A., Maeyama, S., Watanabe, T.-H., Sugama, H., and Nakajima, N., Nuclear Fusion **53**, (2013) 053007.
[11] Baumgaertel, J. A., Hammett, G. W., and Mikkelsen, D. R., Phys. Plasmas 20, (2013) 022305.
[12] Ishizawa, A., Watanabe, T.-H., Sugama, H., Maeyama, S., and Nakajima, N., Phys. Plasmas **21**, (2014) 055905.
[13] Ishizawa, A., Maeyama, S., Watanabe, T.-H., Sugama, H., and Nakajima, N., to appear Journal of Plasma Physics (2015).
[14] Jenko, F. and Dorland, W., Plasma Physics and Controlled Fusion **43**, A141 (2001).
[15] Candy, J. and Waltz, R. E., Journal of Computational Physics **186**, 545 (2003).
[16] Candy, J., Phys. Plasmas **12**, 072307 (2005).
[17] Waltz, R. E., Candy, J., and Faheyc, M., Phys. Plasmas 14, 056116 (2007).
[18] Pueschel, M. J., Kammerer, M., and Jenko, F., Phys. Plasmas **15**, 102310 (2008).
[19] Gorler, T. and Jenko, F., Phys. Rev. Lett. 100, 185002 (2008)
[20] Told, D., Jenko, F., Xanthopoulos, P., et.al., Phys. Plasmas 15 , 102306 (2008)
[21] Peeters, A. G., Camenen, Y., Casson, F. J., et.al., Computer Physics Communications 180, 2650 (2009).
[22] Pueschel, M. J. and Jenko, F., Phys. Plasmas **17**, 062307 (2010).
[23] Waltz, R. E., Phys. Plasmas **17** 072501 (2010).
[24] Guttenfelder, W., Candy, J., Kaye, S. M., et.al., Phys. Rev. Lett. 106, 155004 (2011)
[25] Hatch, D. R., Pueschel, M. J., Jenko, F., Phys. Rev. Lett. **108**, 235002 (2012).
[26] Pueschel, M. J., Gorler, T., Jenko, F., et.al., Phys. Plasmas 20, 102308 (2013).
[27] Gorler, T., White, A. E., Told, D., Jenko, F., Holland C., and Rhodes, T. L., Phys. Plasmas 21 , 122307 (2014)
[28] White, A. E., Schmitz, L., McKee, G. R., et.al., Phys. of Plasmas 15 056116 (2008)
[29] Holland, C., White, A. E., McKee, G. R., et.al.,Physics of Plasmas 16 052301 (2009)
[30] Told, D., Jenko, F., Gorler, T., Casson, F. J., Fable, E., and ASDEX Upgrade Team, Phys. Plasmas 20 , 122312 (2013)
[31] Kaneko, O., Yamada, H., Inagaki, S., and LHD Experiment Group, Nuclear Fusion 53 (2013) 104015.
[32] Baumgaertel, J. A., et.al., Phys. Plasmas 19, (2012) 122306

ρ	$1/L_n$	$1/L_{Ti}$	$1/L_{Te}$	$\hat{s}$	$\beta_i[\%]$	q
0.46	-0.52	7.9	4.6	-0.53	0.19	2.2
0.65	-0.90	12.	9.0	-1.1	0.15	1.7
0.83	3.0	17.	17.	-1.8	0.095	1.2

Table 1. Parameters of LHD #88343 at $t = 2.2$ for $\rho = 0.46$, 0.65, and 0.83.

[33] Angioni, C., Candy, J., Fable, E., et.al., Phys. Plasmas 16, 060702 (2009)
[34] Tanaka, K., et.al., Plasma and Fusion Research 5, (2010) S2053.
[35] Hirshman, S.P. and Betancourt, O., J. Comput. Phys. 96, (1991) 99.
[36] Tang, W. M. ,Connor, J. W., Hastie, R. J., Nucl. Fusion **20**, (1980) 1439.
[37] Kim, J.Y., Horton, W., and Dong, J. Q., Phys. Fluids **B 5**, (1993) 4030.
[38] Sugama, H. and Watanabe, T.-H., Phys. Plasmas **11**, (2004) 3068.
[39] Beer, M. A., Cowley, S. C., and Hammett, G. W., Phys. Plasmas **2**, (1995) 2687.
[40] Watanabe, T.-H. and Sugama, H., Nuclear Fusion **46**, (2006) 24.
[41] Maeyama, S., Ishizawa, A., Watanabe, T.-H., Nakajima, N., Tsuji-Iio, S. and Tsutsui, H., Computer Physics Communications, 184, (2013) 2462.
[42] Sugama, H., Watanabe, T.-H., Nunami, M., Phys. Plasmas **16** (2009) 112503.
[43] Dimits, A. M., et. al., Phys. Plasmas 7, 969 (2000).
[44] Sugama, H. and Watanabe, T.-H., Phys. Rev. Lett. 94, 115001 (2005).
[45] Sugama, H. and Watanabe, T.-H., Phys. Plasmas 13, 012501 (2006).

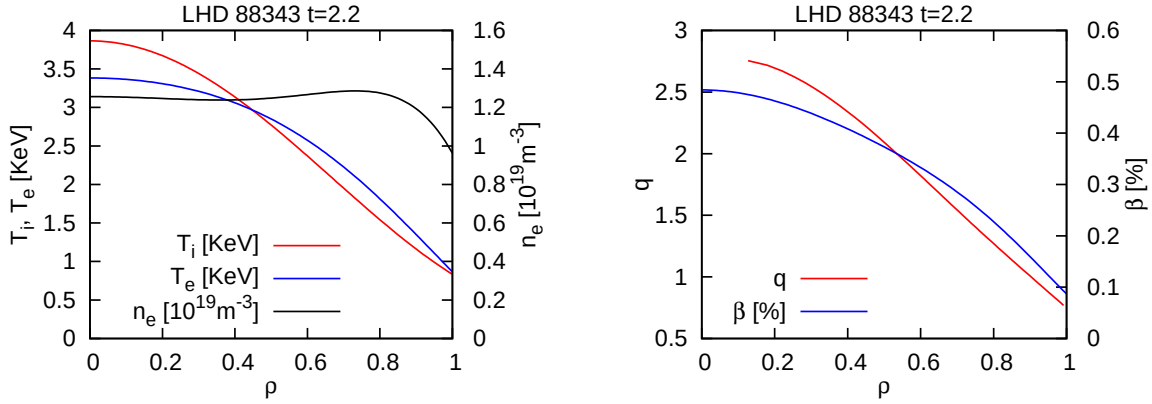

Figure 1. Radial profiles of ion temperature T_i, electron temperature T_e, electron density n_e, safety factor q, and plasma beta β at $t = 2.2$ of the high ion temperature discharge LHD 88343.

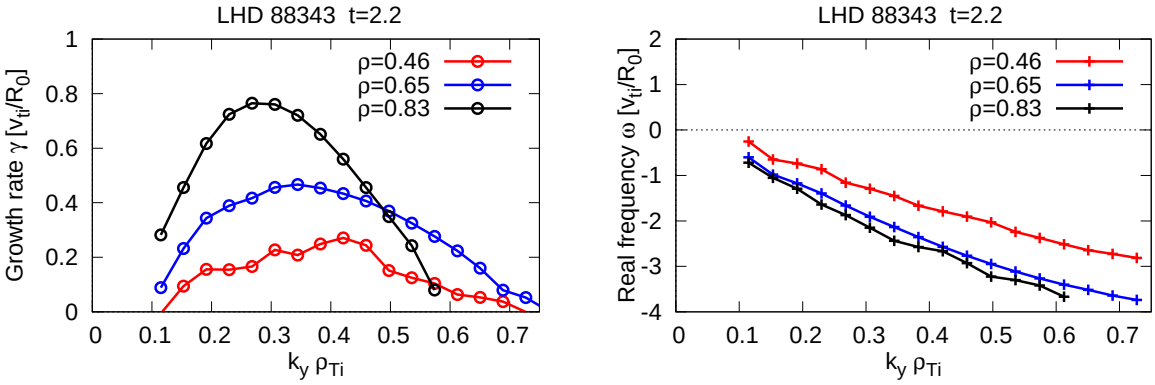

Figure 2. Growth rate and real frequency of the micro-instability at $t = 2.2$ in LHD 88343 as a function of binormal wavenumber k_y. The irregular features at position $\rho = 0.46$ are presently not well-understood and require further study.

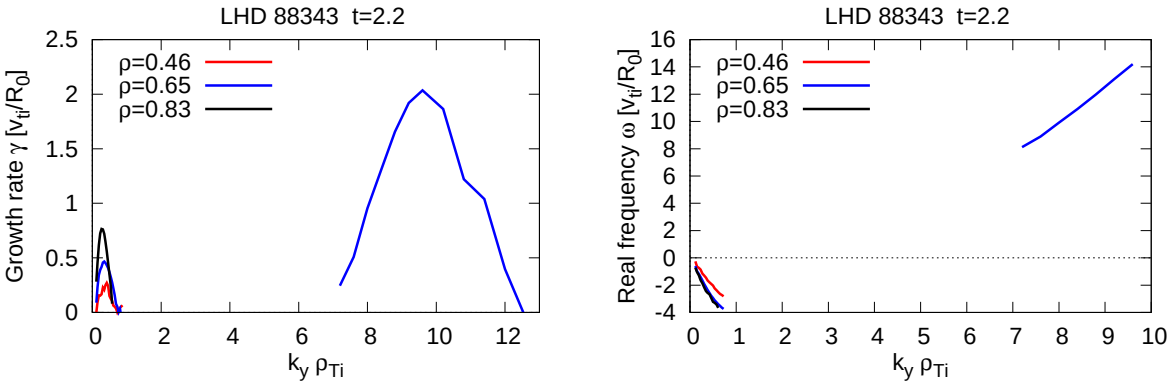

Figure 3. Growth rate and real frequency of the micro-instability at $t = 2.2$ in LHD 88343 as a function of binormal wavenumber k_y.

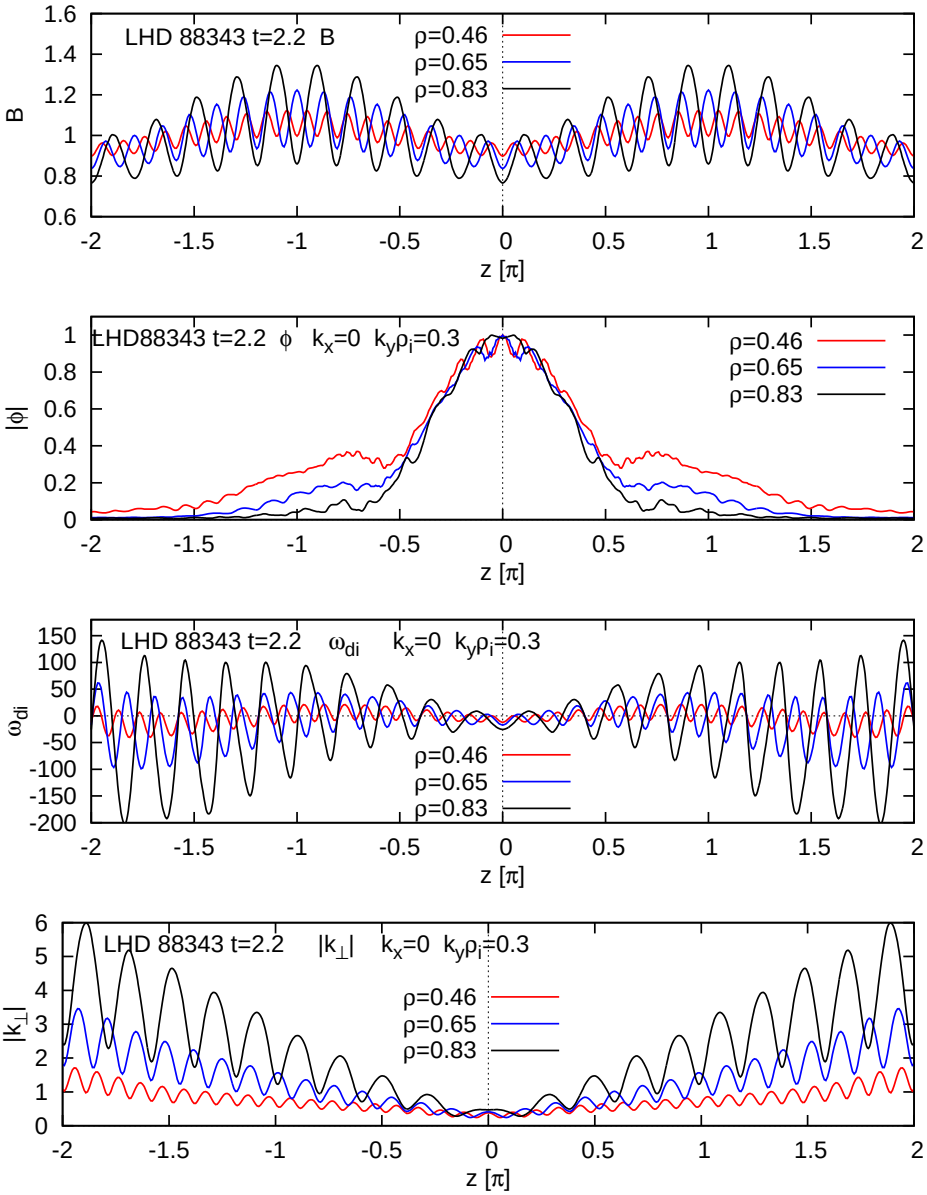

Figure 4. Profiles of the amplitude of magnetic field B, the electrostatic potential ϕ, the magnetic drift frequency $\omega_{di} = \mathbf{v}_{di} \cdot \mathbf{k}_\perp$, and the norm of the perpendicular wavenumber $|\mathbf{k}_\perp|$ for $(k_x, k_y) = (0, 0.3/\rho_{Ti})$ along the magnetic field line at $\rho = 0.46$, 0.65, and 0.83.

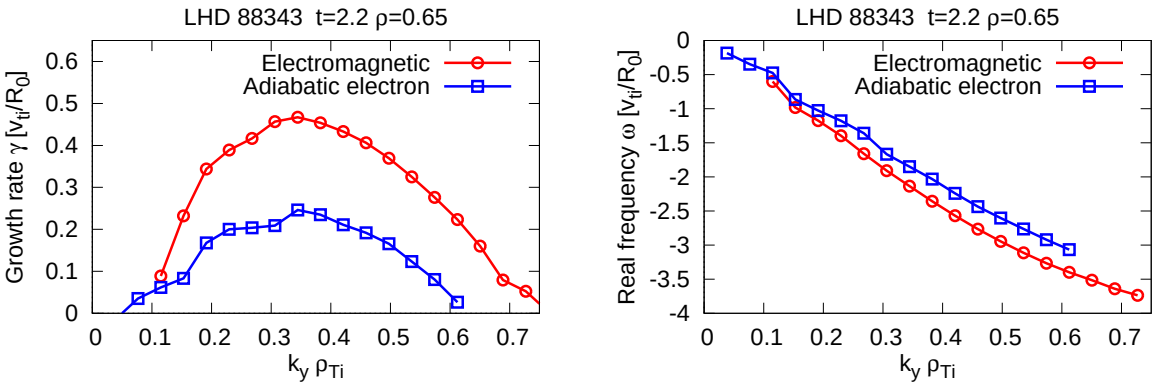

Figure 5. Growth rate and real frequency of the micro-instability at $\rho = 0.65$ and $t = 2.2$ in LHD 88343 as a function of binormal wavenumber k_y.

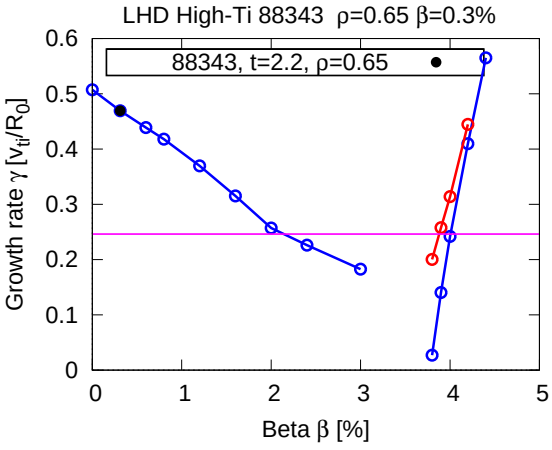

Figure 6. Growth rate as a function of β for LHD 88343. The black point shows that the ITG mode is unstable for the experimental value of beta. The blue open circles show that the ITG mode is suppressed by increasing β with the same magnetic configuration and profiles, and also show that the KBM is destabilized at high beta. The horizontal cyan line denotes the growth rate for the adiabatic electron calculation. The red open circles show the growth rate of instabilities with finite ballooning angles.

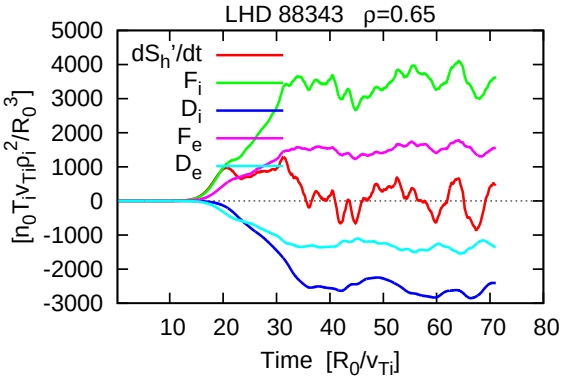

Figure 7. Time evolution of each term in the entropy balance equation, where $S'_h = (\sum_s \delta S_s^{(h)} + W_{es}^{(h)} + W_{em})$.

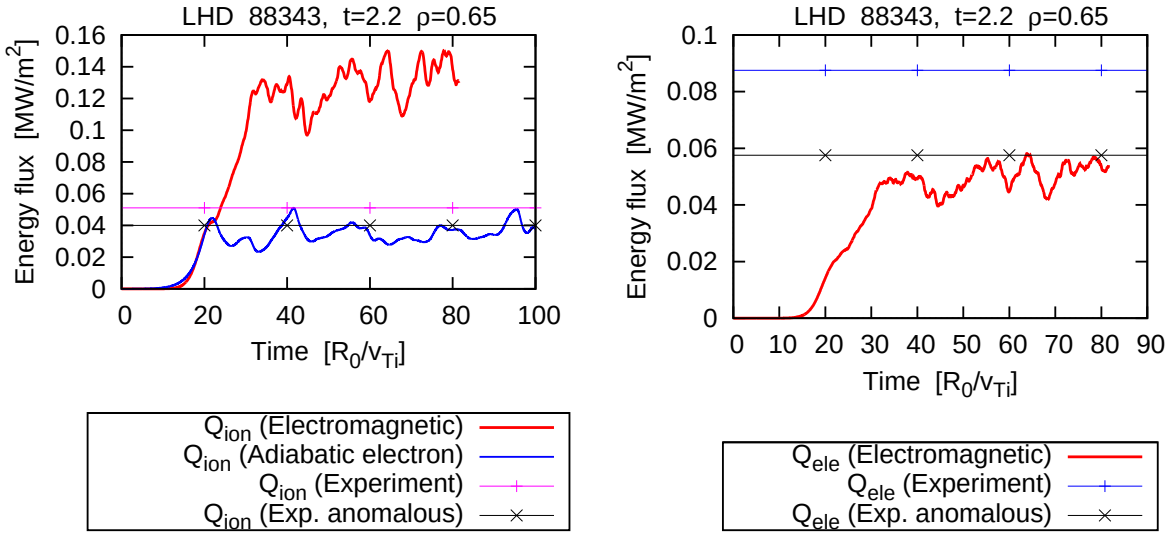

Figure 8. Time evolution of the ion and electron energy fluxes, Q_i and Q_e.

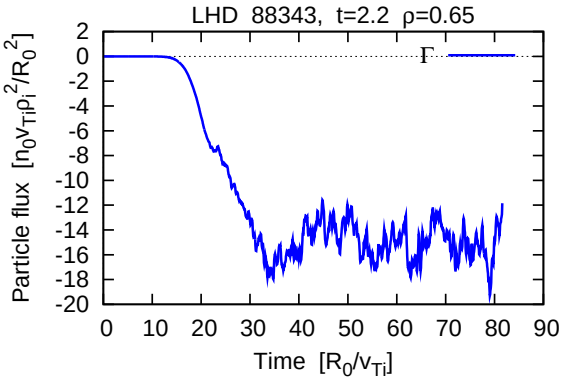

Figure 9. Time evolution of the particle flux $\Gamma = \Gamma_i = \Gamma_e$.

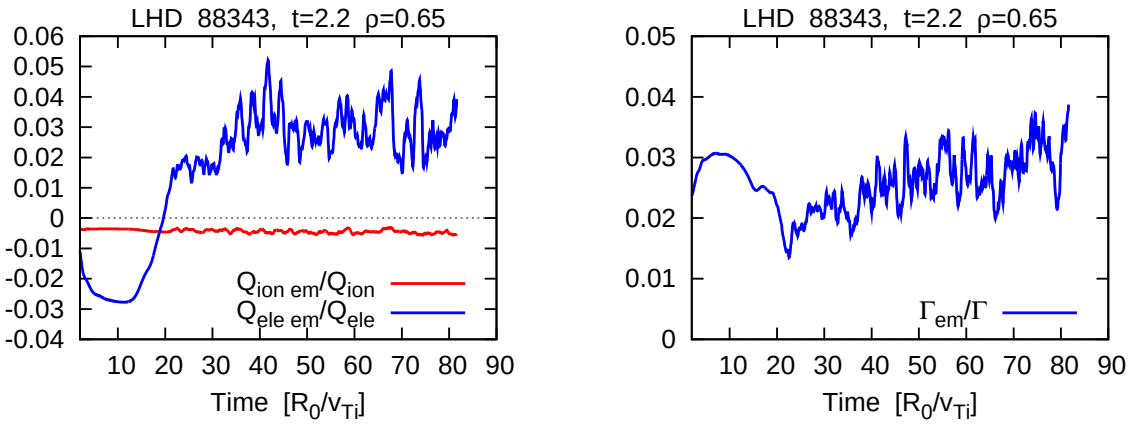

Figure 10. The contribution of magnetic perturbation to the ion and electron energy fluxes and to the particle flux.

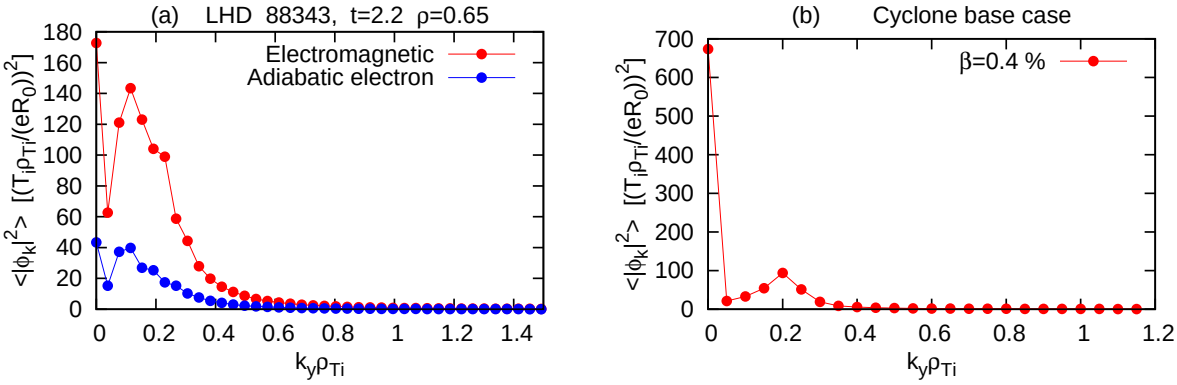

Figure 11. Spectrum of the square of electrostatic potential averaged over the steady state for (a) LHD 88343 $t = 2.2$ and for (b) Cyclone base case tokamak ($\beta = 0.4\%$).

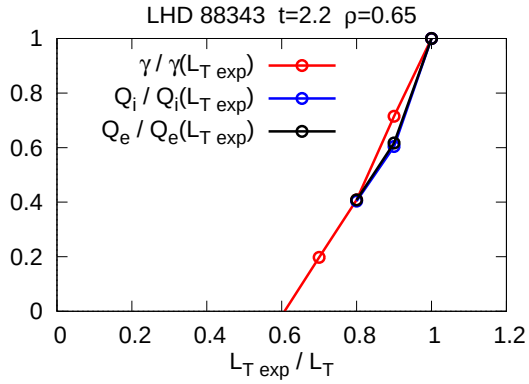

Figure 12. The energy fluxes and the linear growth rate as a function of reduced temperature gradient normalized by the experimental value, $L_{Texp}/L_T \equiv L_{Texp,i}/L_{Ti} = L_{Texp,e}/L_{Te}$. The red line is the linear growth rate, and the blue (black) line represents the ion (electron) energy flux.